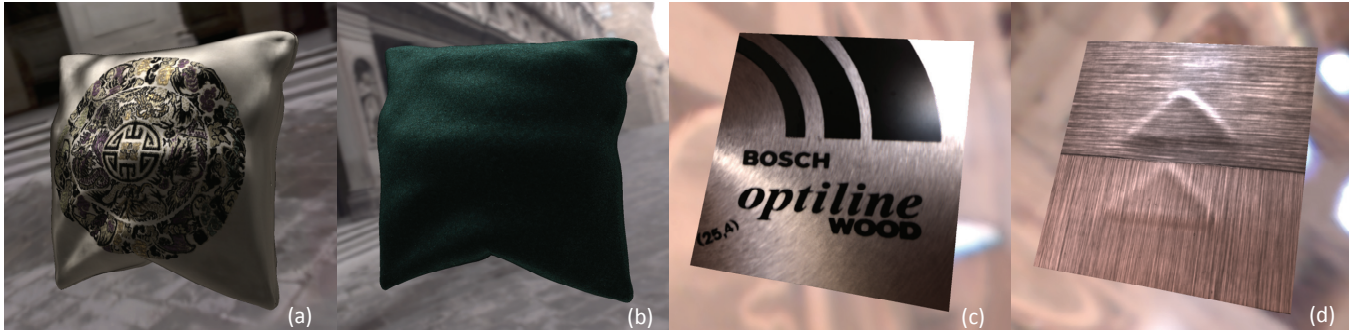


# Reflectance Scanning: Estimating Shading Frame and BRDF with Generalized Linear Light Sources

Guojun Chen<sup>1</sup> Yue Dong<sup>2</sup> Pieter Peers<sup>3</sup> Jiawan Zhang<sup>1</sup> Xin Tong<sup>2,1</sup>  
<sup>1</sup>Tianjin University <sup>2</sup>Microsoft Research <sup>3</sup>College of William & Mary



**Figure 1: Rendering of SVBRDFs reconstructed by our method.** (a) Satin with complex needlework. (b) Velvet with complex reflectance. (c) Brushed metal exhibiting rich tangent variations. (d) Anisotropic paper with bumpy geometric details.

## Abstract

We present a generalized linear light source solution to estimate both the local shading frame and anisotropic surface reflectance of a planar spatially varying material sample.

We generalize linear light source reflectometry by modulating the intensity along the linear light source, and show that a constant and two sinusoidal lighting patterns are sufficient for estimating the local shading frame and anisotropic surface reflectance. We propose a novel reconstruction algorithm based on the key observation that after factoring out the tangent rotation, the anisotropic surface reflectance lies in a low rank subspace. We exploit the differences in tangent rotation between surface points to infer the low rank subspace and fit each surface point’s reflectance function in the projected low rank subspace to the observations. We propose two prototype acquisition devices for capturing surface reflectance that differ on whether the camera is fixed with respect to the linear light source or fixed with respect to the material sample.

We demonstrate convincing results obtained from reflectance scans of surfaces with different reflectance and shading frame variations.

**CR Categories:** I.3.7 [Computer Graphics]: Three-Dimensional Graphics and Realism—Rendering

**Keywords:** BRDF, anisotropic, linear light source

**Links:** [DL](#) [PDF](#) [DATA](#)

## 1 Introduction

Digitally reproducing the visual richness of the appearance of real-world materials is a challenging and important problem in computer graphics. Recent developments in measurement-based appearance modeling have produced more convenient, more robust, and more portable techniques for capturing isotropic surface reflectance. However, robustly characterizing spatially varying *anisotropic* surface reflectance and the local shading frame remains largely an open problem.

In contrast to spatially varying isotropic surface reflectance acquisition methods, only a handful of practical methods for characterizing spatially varying *anisotropic* surface reflectance have been developed. Existing methods either rely on analytical surface reflectance models [Aittala et al. 2013; Ghosh et al. 2009; Tunwattanapong et al. 2013] or require a dense sampling in both the spatial and the angular domain [Wang et al. 2008; Dong et al. 2010]. The former is limited by the representational power of the analytical models and it can fail to accurately characterize complex anisotropic materials such as velvet. The latter often requires complex acquisition setups and its accuracy is limited by the acquisition effort – accurately modeling sharp specular surface reflectance requires very dense sampling.

In this paper we introduce a novel generalized linear light source reflectometry framework for reconstructing spatially varying *anisotropic* surface reflectance and accurate local shading frames from reflectance observations of scanning three intensity-modulated linear sources – a constant linear light source and two phase-shifted sinusoidally modulated linear light sources – over the reflectance sample. Our framework, in concert with a novel data-driven reflectance representation, supports a broad range of surface reflectance properties ranging from diffuse to sharp specular materials, while minimizing acquisition cost without sacrificing accuracy. A key observation is that local shading frame alignment (a non-linear transformation) projects the global anisotropic appearance subspace into a lower rank subspace. This observation suggests that separating shading frame estimation and reflectance modeling can reduce acquisition complexity. We exploit the spatial variation of local shading frames to aid in inferring the low rank linear appearance subspace in the canonical shading frame, and estimate both the

local shading frame as well as the location in the linear appearance subspace of each surface point’s BRDF.

We demonstrate the effectiveness of our framework using two novel generalized linear light source reflectometers comparable in form and usage to a desktop document scanner and a handheld document scanner respectively. We validate the accuracy and robustness of our framework on a variety of different spatially varying materials.

In summary, our contributions are:

- a generalized linear light source reflectometry framework with an  $O(N)$  acquisition complexity (compared to  $O(N^2)$  for competing direct sampling methods such as [Wang et al. 2008]);
- a novel reflectance reconstruction algorithm based on a flexible data-driven microfacet reflectance model that takes as input projections of anisotropic surface reflectance with unknown relative shading frames;
- a compact set of sinusoidal linear light source conditions that support robust estimation of local shading frames and surface reflectance; and
- two practical generalized linear light source reflectometer designs that are compatible with desktop and handheld document scanner form factors.

## 2 Related Work

Measurement-based reflectance modeling techniques can roughly be categorized based on their acquisition strategy: direct sampling methods, and methods that employ complex lighting patterns.

**Direct Sampling** Direct sampling methods probe the appearance of a material sample from multiple viewpoints and multiple lighting directions. It is a natural and straightforward acquisition strategy that only requires moving a camera and/or a light source, and it aligns best with classical sampling theory. Several strategies have been employed to sample different view and lighting directions, ranging from full mechanical positioning using a gonireflectometer [Dana et al. 1999; Lawrence et al. 2006], to specialized devices that eliminate mechanical motion of view and/or lighting [Han and Perlin 2003; Mukaigawa et al. 2007; Ben-Ezra et al. 2008]. However, these acquisition methods densely sample view and lighting directions, and are consequently time-consuming. The captured data is directly used or fit to an analytical reflectance model.

To reduce acquisition cost, several methods share reflectance information across different surface points. Image-based approaches [Marschner et al. 1999; Lu et al. 1998; Matusik et al. 2003] capture the surface reflectance of a homogeneous convex object from a fixed viewpoint, and rely on normal variations between surface points to sample the surface reflectance sufficiently. Zickler et al. [2005] share reflectance information over view, lighting, and surface, and treat the reconstruction of the reflectance as a scattered-data interpolation problem by assuming smooth variation over the space. Lensch et al. [2003] and Goldman et al. [2005] model spatially varying surface reflectance of an object of known geometry as a linear combination of a set of *basis* materials modeled by a Lafortune [Lafortune et al. 1997] and isotropic Ward [1992] reflectance model respectively. Alldrin et al. [2008] infer reflectance and geometry simultaneously. They model the surface reflectance as a linear combination of basis functions, but recognize the limitations of using an analytical model for describing surface reflectance, and instead employ a data-driven bivariate function. All of these techniques are restricted to isotropic surface reflectance, and cannot be easily extended to accommodate anisotropic reflectance.

Wang et al. [2008] model anisotropic surface reflectance using a general microfacet model from single-view observations under a dense sampling of lighting directions. Because only a partial microfacet distribution can be directly recovered from the measurements, Wang et al. gather information from overlapping microfacet distributions to infer a complete microfacet distribution per surface point. Manifold bootstrapping [Dong et al. 2010] employs a two-phase acquisition scheme to estimate spatially varying anisotropic surface reflectance. A specialized device directly captures the surface reflectance at a moderate number of surface points, from which the appearance manifold is computed. In a second step a sparse sampling of lighting directions provides a mapping for each surface point to a point on the appearance manifold. Both methods handle anisotropic reflectance by extending the representative set to include rotated versions, and then find the best match in the global shading frame. The proposed method, in contrast, exploits reflectance coherence between surface points with different shading frame orientations to obtain a more compact appearance space, and thus a more efficient acquisition.

Holroyd et al. [2008] estimate per-surface point shading frames by exploiting symmetries across the normal-tangent and normal-binormal planes. However, to accurately estimate shading frames, a dense sampling of lighting directions is needed. The proposed method, on the other hand, can estimate local shading frames from a sparse set of measurements.

**Complex Lighting Patterns** An alternative acquisition strategy to taking point samples of surface reflectance, is to record the responses of surface reflectance under complex lighting patterns. This corresponds to observing the inner-product of the incident lighting with the reflectance functions.

Ghosh et al. [2009] and Tunwattanapong et al. [2013] extend the polarized spherical gradient method of Ma et al. [2007] to estimate surface shape, specular and diffuse albedo, local shading frame, and anisotropic roughness parameters. Both methods rely on a fragile inverse lookup based on an analytical proxy model to relate the observed radiance to model parameters. The result of such an inverse lookup can be unpredictable when the surface reflectance lies outside the space spanned by the analytical model. In contrast, the proposed method employs a flexible data-driven model that spans a significantly larger appearance space.

Aittala et al. [2013] present a practical method for SVBRDF capture that only uses low-cost commodity parts. Key to their method is the tight coupling between the design of the acquisition lighting and the reflectance model. Similar to us, Aittala et al. also rely on Gaussian models to reduce the degrees of freedom. While their method requires very few illumination patterns (and thus measurements), it is, in contrast to our method, limited to isotropic reflections only.

The acquisition setups of Gardner et al. [2003] and Ren et al. [2011] are most similar to ours. Similar to us, both Gardner et al. and Ren et al. scan a linear light source over the material sample. Using a linear light source has the advantage that it increases the likelihood of capturing the specular peak response and, simultaneously, decreases the acquisition complexity. However, both Gardner et al.’s and Ren et al.’s method are limited to isotropic surface reflectance only. In contrast, the proposed method follows a significantly different reconstruction strategy based on a sample-specific appearance subspace using a more expressive data-driven representation for *anisotropic* surface reflectance. Furthermore, to reconstruct the appearance subspace and estimate local shading frames, we use sinusoidal intensity-modulated linear light sources in addition to Gardner et al.’s and Ren et al.’s constant-intensity linear light source.

### 3 Acquisition Devices

The reflectance behavior at a surface point is described by the 4D Bidirectional Reflectance Distribution Function (BRDF) [Nicodemus et al. 1977] that expresses the ratio of exitant radiance to incident irradiance. In this paper we assume that the anisotropic surface reflectance can be accurately modeled using microfacet theory, reducing the estimation from a full 4D BRDF to the estimation of a 2D microfacet normal distribution function (NDF). Our goal is to estimate this NDF for each surface point of a planar spatially varying anisotropic material.

Accurately handling sharp specular reflections requires a dense angular sampling of the incident or outgoing light field. Point-sample based methods, such as [Wang et al. 2008], typically have an acquisition complexity of  $O(N^2)$ , and do not scale well to dense sampling rates. Linear light source reflectometry [Gardner et al. 2003; Ren et al. 2011] is an attractive alternative with an  $O(N)$  acquisition complexity, and is well suited to capture sharp specular materials. However, existing linear light source reflectometry methods are limited to isotropic surface reflectance.

We propose to generalize linear light source reflectometry to handle anisotropic reflectance by modulating the illumination along the linear light source according to several modulation patterns. It is straightforward to see that the limit case, where each modulation pattern corresponds to a point light at a different location, reverts to a direct sampling method and thus can characterize anisotropic surface reflectance, but at the cost of increasing the acquisition complexity to  $O(N^2)$ . However, the modulation patterns do not necessarily need to correspond to point samples or linear basis functions, but they can be any lighting pattern. In Section 7 we will introduce a compact set of just 3 modulation patterns—a constant and 2 phase-shifted sinusoids—that allow us to accurately estimate surface reflectance, using the novel reconstruction algorithm presented in Section 5, from spatially varying anisotropic materials, while maintaining an  $O(N)$  acquisition complexity.

**Acquisition Devices** We have built two different generalized linear light source reflectometer prototypes inspired by the form factors of typical document scanners:

1. **Desktop scanner form factor:** This device is an evolution of the classic linear light source reflectometer [Gardner et al. 2003]. The camera observes the SVBRDF from a fixed vantage point while the linear light source is scanned over the sample. Figure 2(a) shows our setup.
2. **Handheld scanner form factor:** In this device the relative positions of the camera and linear light source are fixed, and the sample moves with respect to both (or vice versa). We employ a cylindrical lens to image a single scanline of the material sample from different view directions in a single photograph. In other words, the captured image’s x-coordinate corresponds with surface location directly below the lens, while the y-coordinate varies with view direction (in the plane perpendicular to the scanline). Figure 2(b) shows our setup.

Both devices use the same set of camera, linear light sources, and slider. The camera is a Canon 5D Mark II equipped with an EF 100 F2.8 Micro lens, and the linear light source is based on a 35 cm CCFL typically used for backlighting an LCD display and which is positioned 6 cm above the material sample. We print the modulation function as a transparent mask for the linear light source using a calibrated flatbed UV ink printer, however, other more dynamic solutions such as an LCD array are also possible. The slider is a motorized Linear Slides, Zaber T-LSR300A with a microstep size of  $0.09\mu\text{m}$ , which we use to move the light source (desktop form factor) or to move the sample relative to the camera/light source

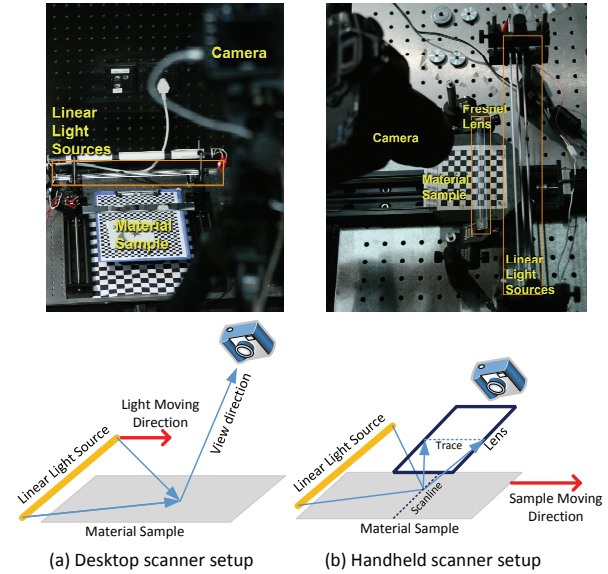


**Figure 2: Acquisition Devices.** (a) Acquisition device inspired by the classical linear light source reflectometer [Gardner et al. 2003]. The linear light source moves relative to the camera, while the camera is fixed with respect to the material sample. (b) Acquisition device inspired by handheld document scanners. The sample moves relative to the camera and light source, and both camera and linear light source are fixed with respect to each other.

(handheld form factor). Finally, for the second device we use an Edmund Optics cylindrical Fresnel lens with a focal length of 0.25”, yielding a view angle range of about 50 degrees.

Our prototype devices use multiple linear light sources (each with a different modulation pattern) and perform a separate scanning pass for each light source. Ideally, future revisions of the prototype devices would employ a single time-multiplexed linear light source to minimize mechanical translation passes and speed up acquisition. For the desktop scanner form factor with 3 modulation patterns, a single reflectance scan consists of recording 240 single-exposure radiometrically linear RAW images (80 linear light source positions per lighting pattern). For the handheld scanner form factor, the number of recorded images is tailored to the desired number of scanlines.

**Calibration** Both setups only need to be calibrated at construction. The desktop form factor device primarily relies on the repeatability of the slider to avoid recalibration, whereas the handheld form factor device keeps the light source/camera configuration fixed.

We calibrate the camera geometrically using the method of Zhang [2000]. For the handheld device, we also calibrate the transmittance and geometrical distortions of the cylindrical lens by densely sampling a mirrored surface (as SVBRDF) illuminated by a collimated beam with known incident direction.

In addition, we measure the actual emitted radiance for each of the modulated linear light source patterns by scanning a mirrored surface. We measure the luminance along the length of the linear light source for each of the patterns, and model the linear light source as a uniform emitter perpendicular to length of the linear light source. We include the effects of foreshortening and distance-falloff to obtain a physically accurate estimate of the radiance at the observed surface points for each relative linear light source position.

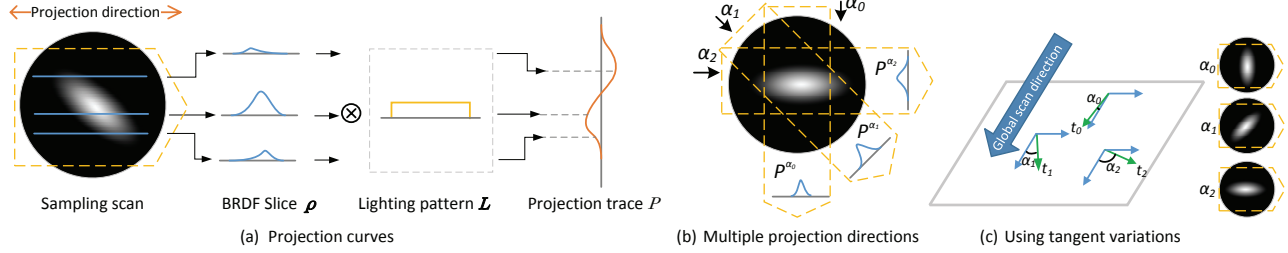


**Figure 3: Reflectance Projection Trace:** (a) A projection trace  $P$  is the projection along a 1D path of the reflectance function modulated by a function  $L$ . (b) The original reflectance function can be reconstructed from a set of projection traces obtained from a sufficiently dense sampling of projection directions. (c) Instead of explicitly sampling multiple projection directions, we exploit variation in the tangent directions between surface points to implicitly sample multiple projection directions.

## 4 Reflectance Model

**Projection Traces** Both acquisition devices presented in Section 3 produce a 1D sequence of measurements for each surface point per modulation pattern. For the desktop scanner, this sequence is obtained by observing the temporal change (i.e., for each linear light source position) of a camera pixel (i.e., surface point). For the handheld scanner, the sequence is obtained from the different views of a surface point (i.e., corresponding y-scanline when the scanner is above the surface point). We denote such a 1D sequence as a projection trace. Formally, the formation of a projection trace can be expressed as:

$$\mathbf{p} = \mathbf{L}\mathbf{r}, \quad (1)$$

where  $\mathbf{p}$  is a vector representing the projection trace discretized in  $m$  steps.  $\mathbf{r}$  is the discretized reflectance function stacked in a  $v$ -length vector.  $\mathbf{L}$  is an  $m \times v$  projection matrix that projects the reflectance function to the projection trace. The exact form of this projection matrix depends on (a) the illumination modulation pattern, and (b) the geometry of the acquisition setup (view and light position). In practice, to compensate for differences between the ideal and actual modulation pattern, we infer  $\mathbf{L}$  from the calibrated radiance of the modulated linear light source (Section 3).

To illustrate Equation (1), consider the following simplified case where we directly work on the 2D NDF domain, and ignore masking, shadowing and Fresnel reflectance. Furthermore, let us assume that the illumination function is a constant function and that the projection of the linear light source onto the NDF domain corresponds to a line that moves for the different observations in a perpendicular direction (i.e., moving the linear light source corresponds to moving the projected line in the NDF domain). Thus, each observation corresponds to the integral of the NDF over a line, or the projection trace corresponds to the projection of the NDF along the direction of the projected line (Figure 3.a). This is akin to the Radon transform, and can be easily inverted if a sufficiently dense sampling of *projection directions* is available (Figure 3.b). This suggests that surface reflectance can be recovered by scanning the material sample along many directions (assuming perfect alignment between the scans). However, such an approach is not practical and would increase the acquisition complexity to  $O(N^2)$ . A key observation is that instead of explicitly sampling multiple projection directions, we can exploit the natural variation in tangent directions between surface points to implicitly sample projection directions (Figure 3.c). While conceptually straightforward for homogeneous materials, it is less obvious how to exploit this observation for spatially varying materials where the observations of each surface point are projections with an unknown projection direction of potentially different reflectance functions.

**Representative BRDFs** Prior work has shown that the appearance space spanned by a spatially varying material can be efficiently modeled by a hyperplane [Lawrence et al. 2006] for isotropic BRDFs, and a low-dimensional manifold [Dong et al. 2010] for isotropic and anisotropic BRDFs. However, for anisotropic reflectance we posit that the main source of non-linearity of the manifold is due to the tangent rotation. Similarly to isotropic BRDFs, the appearance space for a fixed tangent direction can be efficiently modeled by a *linear* low rank subspace. We will therefore model the appearance space of spatially varying materials as a *linear subspace* formed by a set of representative BRDFs in the canonical tangent frame, and include the tangent transformation separately:

$$\mathbf{r} = \mathbf{T}(t)\mathbf{B}\mathbf{w}_b, \quad (2)$$

where  $\mathbf{B}$  is a  $v \times b$  matrix of  $b$  representative (basis) BRDFs,  $\mathbf{w}_b$  are the respective weights, and  $\mathbf{T}(t)$  the  $v \times v$  matrix that transforms the resulting reflectance vector into the tangent frame (from the canonical frame).

We can extend Equation (2) for a single surface point to compactly describe the SVBRDF over multiple ( $p$ ) surface points:

$$\mathbf{R} = \mathbf{T}(t)\mathbf{B}\mathbf{W}_b, \quad (3)$$

where  $\mathbf{R}$  is a  $v \times p$  matrix (each column corresponds to a surface point's reflectance function  $\mathbf{r}$ ), and  $\mathbf{W}_b$  are the corresponding weights ( $b \times p$  matrix). For compactness, we abuse notation for  $\mathbf{T}(t)$  which is not a fixed matrix as in Equation (2), but a matrix-valued function that varies depending on which surface point we are computing – each surface point can have a different tangent  $t$ .

Similarly, we can also extend Equation (1) to describe the projection trace observations over the SVBRDF:  $\mathbf{P} = \mathbf{L}\mathbf{R}$ .

**Gaussian Mixture Model** Given the reflectance projection traces  $\mathbf{P}$  for each surface point of the material sample, our goal is to infer the shading frames  $t$ , the weights  $\mathbf{W}_b$  and the representative BRDFs  $\mathbf{B}$ .

As noted before, we assume an underlying microfacet BRDF model for  $\mathbf{B}$ . In particular we employ a Cook-Torrance BRDF model [Cook and Torrance 1982] with a data-driven microfacet distribution. However, pure data-driven (i.e., tabulated) **2D NDF models** have too many degrees of freedom to reliably solve from the sparse set of **1D reflectance traces**. Instead we propose to employ a novel data-driven Gaussian mixture model for representing the NDFs:

$$\mathbf{B} = \mathbf{G}\mathbf{W}_g, \text{ s.t. } \mathbf{W}_g \geq 0. \quad (4)$$

Each column in  $\mathbf{G}$  contains a discretization (similar to  $\mathbf{r}$ ) of an atomic Cook-Torrance BRDF, i.e., where the data-driven NDF is

formed by a single Gaussian (with varying position and standard deviation). Hence,  $\mathbf{G}$  forms a dictionary of atomic BRDFs. Also note that each column of  $\mathbf{G}$  contains the discretization of the micro-facet BRDF and thus includes shadowing, masking and Fresnel effects (i.e., the aggregate reflectance effect of the data-driven NDF). We constrain the weights  $\mathbf{W}_g$  to be non-negative to avoid negative probabilities in the NDF. Furthermore, we add a Lambertian BRDF to  $\mathbf{G}$  to model diffuse reflections accurately.

Including all possible atomic BRDFs (i.e., all possible positions and sizes of the NDF Gaussians), in  $\mathbf{G}$  is impractical. This raises the question of which atomic BRDF to include in  $\mathbf{G}$ . On one hand we want to maximize the representational power, and thus include as many atomic BRDFs as possible in  $\mathbf{G}$ . On the other hand we want to maximize the stability of the estimation of the BRDFs from as few as possible measurements. This implies that the number of coefficients (and thus atomic BRDFs in  $\mathbf{G}$ ) should be minimized. Instead of fixing the content of the dictionary beforehand (with the exception of the Lambertian BRDF), we will include this as a variable in the estimation process.

## 5 Reflectance Reconstruction

Our goal is to reconstruct the SVBRDF from the observations of reflectance projection traces:

$$\operatorname{argmin}_{\mathbf{R}} \|\mathbf{P} - \mathbf{L}\mathbf{R}\|^2. \quad (5)$$

Applying the representative BRDF assumption (Equation (3)) modeled by the data-driven Gaussian Mixture Model (Equation (4)) yields the following minimization target:

$$\operatorname{argmin}_{\mathbf{W}_b, \mathbf{W}_g, t, \mathbf{G}} \|\mathbf{P} - \mathbf{L}\mathbf{T}(t)\mathbf{G}\mathbf{W}_g\mathbf{W}_b\|^2. \quad (6)$$

We posit that  $\mathbf{W} = \mathbf{W}_g\mathbf{W}_b$  must be a low rank matrix, as we desire few representative BRDFs and thus a low rank appearance space. We therefore constrain the above minimization as:

$$\operatorname{argmin}_{\mathbf{W}, t, \mathbf{G}} \|\mathbf{P} - \mathbf{L}\mathbf{T}(t)\mathbf{G}\mathbf{W}\|^2 + \lambda \operatorname{rank}(\mathbf{W}) \quad \text{s.t. } \mathbf{W} > 0, \quad (7)$$

We enforce  $\mathbf{W}$  to be non-negative to avoid negative values in the NDF. Note that  $\mathbf{W}_g$  and  $\mathbf{W}_b$  can be recovered from  $\mathbf{W}$  via a (non-negative) low-rank decomposition (e.g., using ACLS [Lawrence et al. 2006] with non-negativity and sparsity constraints). A common practice in rank minimization problems is to replace the ‘‘rank’’ operator by the nuclear norm  $\|\cdot\|_*$  [Liu et al. 2013]:

$$\operatorname{argmin}_{\mathbf{W}, t, \mathbf{G}} \|\mathbf{P} - \mathbf{L}\mathbf{T}(t)\mathbf{G}\mathbf{W}\|^2 + \lambda \|\mathbf{W}\|_* \quad \text{s.t. } \mathbf{W} > 0. \quad (8)$$

Equation 8 is highly non-linear due to the tangent rotation transformation  $\mathbf{T}(t)$  and the dictionary  $\mathbf{G}$ . We therefore, separate the computation of  $\mathbf{W}$ ,  $t$  and  $\mathbf{G}$ , and iteratively solve for one, while keeping the others fixed.

**Solving  $t$ :** When keeping  $\mathbf{W}$  and  $\mathbf{G}$  fixed, we solve for  $t$  for each surface point separately:

$$\operatorname{argmin}_t \|\mathbf{p} - \mathbf{L}\mathbf{T}(t)\mathbf{G}\mathbf{w}\|^2. \quad (9)$$

We minimize this expression by performing a full search through all tangent directions  $t$ . In practice, we search among 360 discretized tangent directions.

**Solving  $\mathbf{W}$ :** Keeping  $t$  and  $\mathbf{G}$  fixed, reduces Equation (8) to a convex problem that can be efficiently solved via an Augmented Lagrange Multiplier (ALM) method [Liu et al. 2013; Nocedal and Wright 2006]. In particular we adapt the inexact ALM solver proposed by Liu et al. [2013]. For this we first introduce the equivalent form with an additional variable  $\mathbf{J} = \mathbf{W}$ :

$$\operatorname{argmin}_{\mathbf{W}} \|\mathbf{P} - \mathbf{L}\mathbf{T}(t)\mathbf{G}\mathbf{W}\|^2 + \lambda \|\mathbf{J}\|_*, \quad \text{s.t. } \mathbf{W} > 0, \mathbf{W} = \mathbf{J}. \quad (10)$$

Next, we replace the  $\mathbf{W} = \mathbf{J}$  constraint by a Lagrange multiplier  $\mathbf{Y}$  and penalty parameter  $\mu > 0$ :

$$\operatorname{argmin}_{\mathbf{W}} \|\mathbf{P} - \mathbf{L}\mathbf{T}(t)\mathbf{G}\mathbf{W}\|^2 + \lambda \|\mathbf{J}\|_* + \operatorname{tr}(\mathbf{Y}^T(\mathbf{W} - \mathbf{J})) + \frac{\mu}{2} (\|\mathbf{W} - \mathbf{J}\|^2), \quad \text{s.t. } \mathbf{W} > 0. \quad (11)$$

This problem is convex (and only has a non-negativity constraint), and can be efficiently solved by alternating between minimizing with respect to  $\mathbf{W}$  and  $\mathbf{J}$  respectively. We solve for  $\mathbf{J}$  using singular value thresholding [Cai et al. 2010], and we solve for  $\mathbf{W}$  using a non-negative  $L_2$  solver. The Lagrange multipliers and penalty parameters can be adjusted according to the classical ALM method [Nocedal and Wright 2006]. Algorithm 1 summarizes the adapted ALM algorithm.

**Data:** measurement  $\mathbf{P}$ , parameter  $\lambda$

**Result:** weight  $\mathbf{W}$

initialization

$\mathbf{W} = \mathbf{J} = 0, \mathbf{Y} = 0, \mu = 0.001, \mu_{max} = 10^6, \rho = 1.1$ , and  $\varepsilon = 10^{-8}$

**while** *not converged* **do**

- fix  $\mathbf{W}$  and update  $\mathbf{J}$  by:

$$\operatorname{argmin}_{\mathbf{J}} \frac{1}{\mu} \|\mathbf{J}\|_* + \frac{1}{2} \|\mathbf{J} - \mathbf{W} + \mathbf{Y}/\mu\|^2$$

- fix  $\mathbf{J}$  and update  $\mathbf{W}$  by:

$$\operatorname{argmin}_{\mathbf{W}} \frac{1}{\mu} \|\mathbf{P} - \mathbf{L}\mathbf{T}(t)\mathbf{G}\mathbf{W}\|^2 + \frac{1}{2} \|\mathbf{J} - \mathbf{W} + \mathbf{Y}/\mu\|^2 \quad \text{s.t. } \mathbf{W} > 0$$

- update multiplier:  $\mathbf{Y} = \mathbf{Y} + \mu(\mathbf{W} - \mathbf{J})$

- update penalty:  $\mu = \min(\rho\mu, \mu_{max})$

- check convergence:  $\|\mathbf{W} - \mathbf{J}\|_{\infty} < \varepsilon$

**end**

**Algorithm 1:** Inexact ALM algorithm

**Solving  $\mathbf{G}$ :** Finally, we adjust the dictionary  $\mathbf{G}$  by fixing the weight  $\mathbf{W}$  and tangent  $t$  and solving for the number of Gaussians and their positions and sizes in the NDF domain:

$$\operatorname{argmin}_{\mathbf{G}} \|\mathbf{p} - \mathbf{L}\mathbf{T}(t)\mathbf{G}\mathbf{w}\|^2. \quad (12)$$

This is a problem similar to radial basis function interpolation, except that fitness of the interpolation is computed on projections of the target function and projections of the radial basis function (i.e., Gaussians). We optimize  $\mathbf{G}$  by alternating between (1) optimizing for position and size (keeping the number of Gaussians fixed), and (2) refining (i.e., splitting) Gaussians when the approximation is too coarse. We repeat this process until a maximum number of Gaussians (500) is reached or when the reconstruction error drops below some threshold (0.01).

*Optimize position and size:* We perform a greedy optimization where we tentatively modify each Gaussian in  $\mathbf{G}$  and only effectively apply the change to the Gaussian, that after modification, reduced the error the most. Note that a column of  $\mathbf{G}$  does not contain the Gaussian NDF directly, but the resulting (discretized) BRDF of the Gaussian NDF. To accelerate the optimization, we discretize the positions and sizes of the Gaussians and precompute all BRDFs

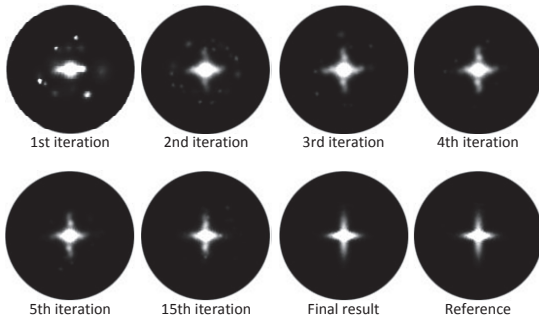


**Figure 4: NDF Evolution.** *Top-left: NDF reconstruction with the initial (randomly assigned) dictionary and shading frame. Middle: the subsequent reconstructions at selected points during the reflectance recovery process. Bottom-right: ground truth NDF.*

(i.e., potential columns). In our implementation we consider 9801 precomputed atomic BRDFs ( $33 \times 33$  discrete positions, and 9 different standard deviations ranging from 0.02 to 0.3 for the Gaussian NDF) with a fixed index of refraction of 1.3. Modifying a Gaussian now becomes replacing it with the next/previous discretized position/size. We repeat this greedy optimization until the error cannot be reduced any further.

*Refinement:* We employ a greedy refinement criterion where we split each Gaussian in  $\mathbf{G}$  and keep the  $K = 10$  splits that reduce the reconstruction error most. We split each Gaussian (with position  $(x, y)$  and size  $\sigma$ ) into 4 smaller Gaussians (with positions  $(x \pm \frac{\sigma}{4}, y \pm \frac{\sigma}{4})$  and size  $\frac{\sigma}{2}$ ), and compute the corresponding optimal weights (Algorithm 1 with the weights of other (unmodified) Gaussians fixed). Thus, each pass increases the number of Gaussians by 30 (i.e.,  $4 \times 10$  new Gaussians minus 10 parent Gaussians).

**Initialization** Our reconstruction algorithm is not particularly sensitive to the initial input. In our implementation we select a random initial tangent direction  $t$  and initialize  $\mathbf{G}$  with 50 Gaussians with random position and size. Given  $t$  and  $\mathbf{G}$  we then start the iterative process by computing the optimal weights  $\mathbf{W}$  (Algorithm 1). Figure 4 shows an example of the evolution of an NDF during the iterative reflectance estimation process.

## 6 Reconstruction Acceleration

Applying the proposed reconstruction algorithm to all surface points is computationally expensive. To speed up the reconstruction computation, we observe that the number of representative BRDFs is low (due to the low rank requirement), suggesting that these representative BRDFs can be estimated from a subset of surface points. To ensure that we select a rich enough subset of surface points, we first perform a  $k$ -means clustering on the observed projection traces  $\mathbf{P}$ , with  $k$  sufficiently large, and select from each cluster (at random) a sample. In our implementation we set  $k$  to 360.

Given the representative BRDFs  $\mathbf{B}$ , we then want to compute the tangent directions  $t$  and weights  $\mathbf{w}_b$  for every surface point. Similarly as for the estimation of the representative BRDFs, we perform an iterative optimization where we alternate between optimizing the tangent direction  $t$  and the BRDF weights  $\mathbf{w}_b$ .

The weights  $\mathbf{w}_b$  are estimated for each surface point by minimizing:

$$\operatorname{argmin}_{\mathbf{w}_b} \|\mathbf{p} - \mathbf{L}\mathbf{T}(t)\mathbf{B}\mathbf{w}_b\|^2 \text{ s.t. } \mathbf{w}_b \geq 0. \quad (13)$$

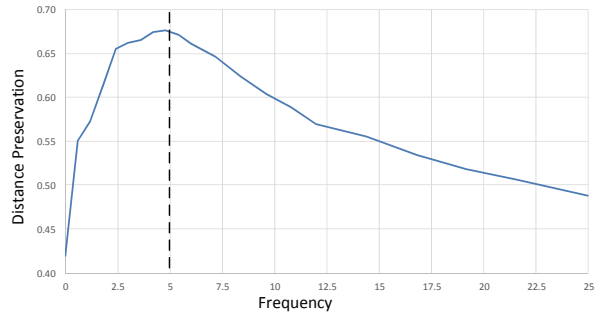
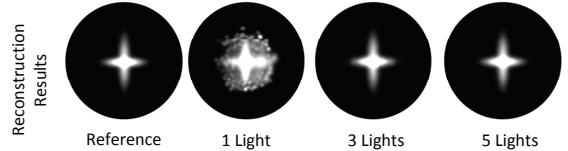
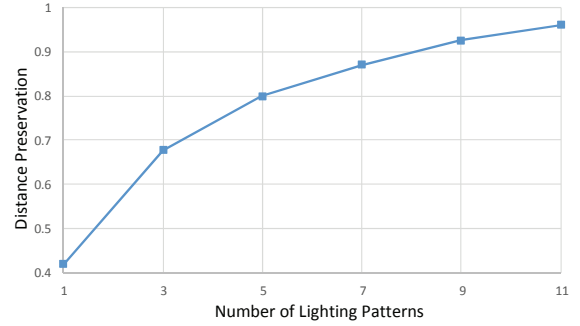


**Figure 5: Lighting Patterns Parameters** *Top: Distance-preservation distance with respect to the number of (phase-shifted sinusoidal) illumination conditions. For each subset the optimal frequencies are chosen (i.e., the combination that resulted in the best distance preservation). Middle: Reconstructions for 1, 3 and 5 illumination patterns. Bottom: Distance-preservation distance with respect to lighting frequency for a pair of phase-shifted sine-wave illumination modulation functions and a constant modulation function*

This minimization problem is convex and can be efficiently computed using a non-negative L2 solver.

To estimate the tangent  $t$  we solve a similar minimization problem:

$$\operatorname{argmin}_t \|\mathbf{p} - \mathbf{L}\mathbf{T}(t)\mathbf{B}\mathbf{w}_b\|^2. \quad (14)$$

As for the representative BRDFs, we solve this by performing a full search through all tangent directions.

## 7 Illumination Design

The reconstruction algorithm introduced in the previous sections requires a sufficiently rich input to accurately reconstruct anisotropic surface reflectance. We aim to design a set of lighting modulation patterns that is small enough to support time-multiplexed acquisition. Ideally, to ensure equal information gain at every surface point, and thus computational robustness, these lighting modulation functions should be translation invariant (i.e., linear combinations of the functions can produce any translated version) over the linear light source.

A well known set of translation invariant functions are phase-shifted sine functions (i.e.,  $\sin(fx)$  and  $\cos(fx)$ , where  $x \in [0, 1]$ )

is the relative position on the linear light source). While practically too large for our purpose, the limit case of using the full set of Fourier basis functions as lighting modulation functions is sufficient to estimate both tangent and reflectance (id. point sampling in the frequency domain). This raises two fundamental questions: (1) what is the minimal number of phase-shifted sine functions, and (2) which are the optimal frequencies to accurately reconstruct surface reflectance.

**Distance Preservation Metric** We adapt the distance preservation metric [Dong et al. 2010] to analyze the effects of different choices on the illumination design. This metric measures how well the projections (under the illumination conditions) preserve the distance between different BRDFs:

$$\tau = \frac{\sum_{i,j} \|\mathbf{P}_i - \mathbf{P}_j\|^2}{\sum_{i,j} \|\mathbf{R}_i - \mathbf{R}_j\|^2}, \quad (15)$$

where  $\mathbf{P}_i$  are the projection traces of the SVBRDF  $\mathbf{R}_i$  under the illumination conditions  $\mathbf{L}$ . We perform our analysis on a representative synthetic dataset of 60,000 BRDFs with an anisotropic Beckman NDF with parameters uniformly sampled ( $\sigma_x \in [0.1, 0.5]$ ,  $\sigma_x/\sigma_y \in [1.0, 5.0]$ , and tangent rotation  $t \in [0, 180]$  degrees).

**Number of Lighting Patterns** Figure 5 (top) plots the distance-preservation distance with respect to the number of illumination modulation functions. By default we include the DC component (a constant function) as one of the lighting conditions, and add pairs of phase-shifted sinusoids with optimal frequency (i.e., that preserve distance best). As expected, the preservation improves with each additional pair. However, at just 3 lighting conditions, our algorithm is already capable of reconstructing the surface reflectance accurately.

**Optimal Frequency** Figure 5 (bottom) plots the distance-preservation distance with respect to frequency for the 3 lighting pattern case (i.e., one constant modulation function, and a pair of phase-shifted sine-wave functions with shared frequency). The simulation conditions match the physical setup (i.e., a 35 cm linear light source suspended 6 cm above the sample surface). We found that under these conditions a frequency of  $f = 5$  provides the best results.

**Finite Linear Light Source Length** We argued for phase-shifted sine modulation functions based on their translation invariant property. In theory these functions extend infinitely in either direction. However, in practice, the length of the modulation function is limited by the length of the linear light source. To better understand the impact of the length limitation on the modulation function, we plot the average difference in projection traces with respect to the ideal infinite illumination condition (Figure 6) on  $10\text{cm} \times 10\text{cm}$  samples of the materials shown in Figures 8 and 14. As can be seen, for the employed 35 cm linear light source, the difference is less than 1%.

**Practical Considerations** We offset the sinusoidal modulation functions to ensure non-negative lighting patterns. Our set of illumination conditions also includes a constant modulation function which, by virtue of linearity of light transport, allows us to undo this offset after capture by simply subtracting the corresponding observed images.

## 8 Full Shading Frame Estimation

Up to this point, we treated the shading frame to be a function of tangent direction only. We extend reflectance scanning to handle

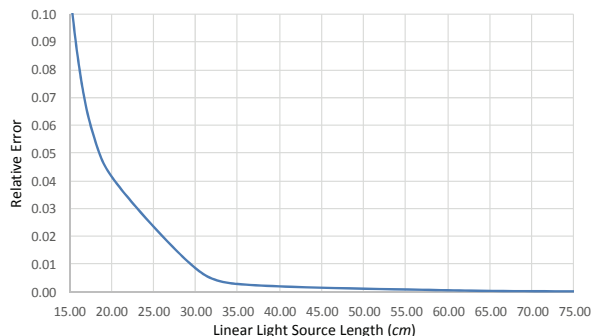


**Figure 6: Impact of Finite Illumination Modulation Functions** The difference in the projection traces obtained from an infinite linear light source and a finite linear light source.

surface normal variations by alternating between estimating surface reflectance and tangent direction (Sections 5 and 6), and refining surface normal. We repeat this process until the change in surface normal is less than 1 degree.

**Surface Normal Refinement** Given converged estimates of the surface reflectance and tangent directions, we search for the surface normal that minimizes the reconstruction error in Equation (5). We first perform a coarse search on a  $257 \times 257$  grid (over  $x$  and  $y$  coordinates) of normal directions. We further refine this estimate by performing a local search in a  $8 \times 8$  grid within the minimizing coarse grid cell. The correctness of the surface refinement process depends on the initial starting normal estimate. We empirically validated that the surface normal refinement converges to the correct normal estimate as long as the initial normal estimate is within 10 degrees of the surface normal.

**Initialization** We estimate the initial normal direction for each surface point by finding the normal that together with an isotropic proxy BRDF (with a single centered Gaussian NDF and a diffuse component) best explains the observed projection traces. Practically, we precompute a table of projection traces for different combinations of normal directions ( $257 \times 257$  grid), diffuse/specular ratios (21 ratios uniformly sampled in  $[0, 1]$ ), and surface roughness (11 uniformly sampled from  $[0.02, 0.2]$ ). We then find the best matching precomputed projection trace using the error metric in Equation (5). Note, we only use the estimated normal, and ignore the estimated diffuse/specular ratio as well as estimated roughness in the remainder of the reflectance reconstruction process.

**Discussion** While we only employ an isotropic proxy BRDF for estimating the initial surface normal, we found that this provides a sufficiently accurate estimate ( $< 10$  degrees) for a wide range of diffuse/specular ratios and roughness for NDFs that decrease monotonically with increasing half-angle. For complex NDFs (e.g., velvet) such a simple isotropic proxy BRDF fails to provide a sufficiently accurate initial surface normal. However, note that in such a case, we can still obtain good reflectance estimates by increasing the number of representative BRDFs and thus include the normal shift in the corresponding NDF estimates.

The effect of the diffuse surface reflectance on the projection traces for the handheld device is a constant offset. Consequently, the estimation of the diffuse/specular ratio becomes ambiguous. Instead, we offset the projection traces by (subtracting) the minimum observed value in the constant illumination projection trace (effect-

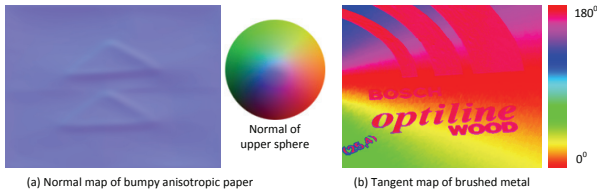


**Figure 7: Shading Frame.** (a) A false color visualization of the recovered normal map for the Bumpy Paper dataset. (b) A false color visualization of the recovered tangent map for the Brushed Metal dataset.

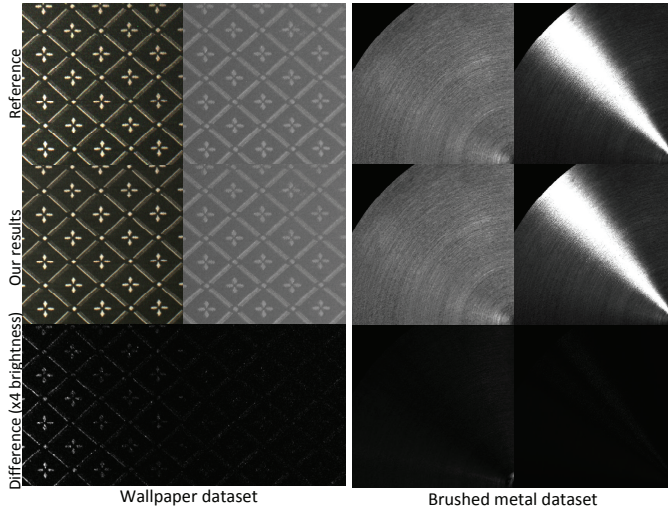


**Figure 8: Validation.** We compare renderings of reconstructed SVBRDFs obtained from simulated measurements on existing datasets. (a) The Wallpaper dataset [Lawrence et al. 2006] consist of both isotropic and anisotropic reflectance. (b) The Brushed Metal dataset [Dong et al. 2010] with sharp anisotropic reflectance and rich tangent variations.

tively removing the diffuse component), and estimate the initial surface normal from specular reflections only.

## 9 Results

**Results** We acquired five datasets exhibiting a wide range of tangent variations (e.g., brushed metal), complex surface reflectance (e.g., velvet and satin), and surface normal variations (e.g., bumpy anisotropic paper). We also show a challenging circle card with rich reflectance details as well as tangent and normal variations. Figures 1 and 14 showcase SVBRDFs acquired using the desktop scanner, and revisualized under complex natural lighting.

The acquisition of the datasets took approximately 1 to 1.5 hours, and required approximately 30GB of storage. We reconstructed 6 representative BRDFs for (a subset of) the Anisotropic Paper to 35 representative BRDFs for (a subset of) the Satin dataset, and which required about 2.5 hours of processing on an Intel Xeon E5-2643 processor with 16GB of memory. Given the representative BRDFs, computing the weights and BRDFs of all surface points (Section 6) took considerably less time (approximately 15 to 45 minutes). We found that the size of the precomputed dictionary of atomic BRDFs (9801), as well as the number of atomic BRDFs (50 to 200 after refinement), were sufficient to accurately represent both rough as well as very sharp specular reflections. Figure 7

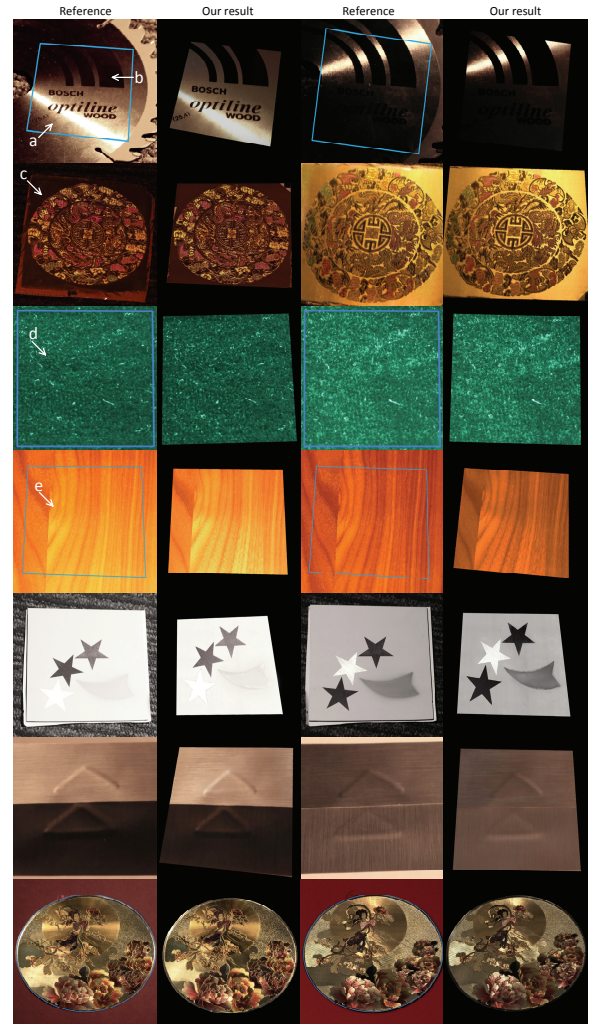


**Figure 9: Ground Truth Comparisons.** Comparison renderings of the reconstructed SVBRDF and two validation photographs. The NDFs of the marked surface points are shown in Figure 10.

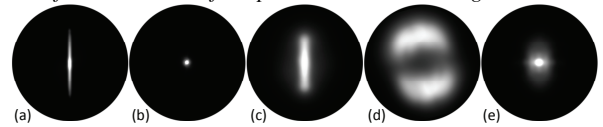


**Figure 10: Reconstructed NDFs** A representative selection of reconstructed NDFs, with varying degrees of complexity, from the spatially varying materials shown in Figure 9.

shows false color visualizations of recovered shading frames. The resulting shading frames are free of artifacts. Full resolution property maps of the diffuse and specular albedo, surface normals, and tangents, as well as the raw input measurements, can be found in the supplementary materials.

**Validation** We validate our method by simulating the acquisition on existing measured datasets: the Wallpaper dataset [Lawrence et al. 2006] and the Brushed Metal dataset [Dong et al. 2010]. Figure 8 compares renderings under two different lighting directions. The reconstructed SVBRDFs produce results qualitatively similar to the ground truth visualizations. Furthermore, we also computed a quantitative error using the BRDF error metric of

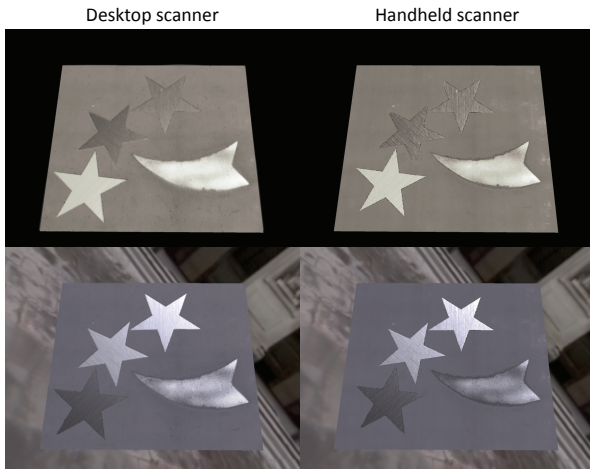


**Figure 11: Acquisition Device Comparison** A comparison between rendering results of reconstructed surface reflectance acquired using the proposed desktop and handheld scanner.

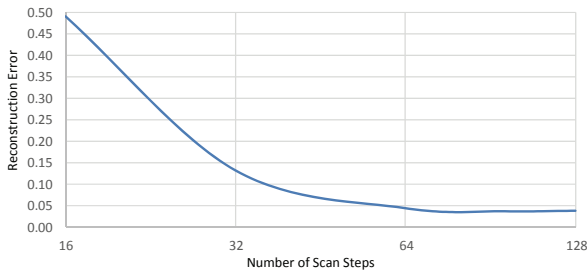


**Figure 12: Sampling rate.** Effect of linear light source position sampling rate on the BRDF reconstruction error [Ngan et al. 2005] on synthetic and measured NDFs.

Ngan et al. [2005]. The error on the Wallpaper dataset is 8.9%, and on the Brushed Metal dataset it is 3.7%.

Figure 9 shows qualitative validations on measured materials captured using the desktop scanner. For each captured dataset, we recorded two additional photographs from a different viewpoint and lit by a point light at different locations. We then compare the capture validation photograph with a visualization of the reconstructed SVBRDF under similar conditions. The reconstructed SVBRDFs produce results visually similar to the ground truth. Figure 10 shows the NDFs of five selected surface points (marked in Figure 9).

Figure 11 demonstrates the reconstruction consistency between the two prototype generalized linear light source reflectometers introduced in Section 3. Both the desktop as well as the handheld scanner produce consistent reconstructions.

**Discussion** Our method relies on having sufficiently rich variation in tangent orientations. However, if this is not the case, then additional scans can be performed in different scan directions by rotating the sample to increase the amount of tangent variation. Note, we only use the rotated scans for reconstructing the representative BRDFs, and the final SVBRDF is reconstructed from a single selected direction. Since the reconstruction of the representative BRDFs does not rely on any spatial order, no fragile and error-prone image registration of the different scan directions is required.

We captured 6 scan directions for the Satin data and 3 directions for the Bumpy Paper dataset to enrich the tangent variations in the measurements. Furthermore, we also validated the stability of the reconstruction with respect to the scanning direction on the brushed metal dataset and reconstructed the surface reflectance for four scan directions at 30, 45, 60, and 90 degrees. We found the differences to be negligible ( $< 0.01$ ), and no structured artifacts were present.

For the desktop scanner, the number of sampled linear light source positions can greatly affect the quality of the reconstructions. We perform an analysis similar to that in Section 7 to determine the optimal sampling rate. Figure 12 plots the average BRDF reconstruction error [Ngan et al. 2005] on datasets of synthetic (Beckman) and measured NDFs. Our analysis shows that 64 samples or higher (on a  $10\text{ cm} \times 10\text{ cm}$  sample, yielding a step size of  $\approx 1.5\text{ mm}$ ) is sufficient for accurate reconstructions.

**Comparison** The method of Wang et al. [2008] can produce similar quality results as ours. However, Wang et al. rely on point sampling incident light positions and therefore have an  $O(N^2)$  acquisition complexity compared to  $O(N)$  for our method which relies on line samples. Because Wang et al. rely on point samples, dense sampling is required to accurately reconstruct sharp specular surface reflectance. Figure 13 compares reconstruction results from our method (using the desktop scanner) and those from Wang et al. [2008] for a simulated acquisition on the Brushed Metal dataset [Dong et al. 2010]. Our method only requires 240 images (80 linear light source positions and 3 illumination modulation functions) to accurately reconstruct the surface reflectance. However, at only 240 samples ( $15 \times 16$ ), Wang et al. fail to reconstruct the surface reflectance faithfully. To achieve similar quality results, they require an order of magnitude more samples (6400 images).

## 10 Conclusion

In this paper we presented “Reflectance Scanning”, a framework for generalized linear light source reflectometry to capture spatially varying anisotropic surface reflectance. A novel reconstruction algorithm was introduced for recovering the microfacet BRDFs and local shading frame from an underconstrained set of reflectance projection traces. A key observation is that when tangent rotation is removed, the resulting appearance space is low rank. We designed two new prototype acquisition devices that are comparable in form to a desktop and a handheld document scanner. Both devices do not require any calibration, except during construction, and together with the recognizable form factor, lowers the threshold for non-expert users to easily model the appearance of complex surface reflectance.

Our current method only works for planar surfaces (i.e., true SVBRDFs). In the presence of large geometric features, occlusion begins to play a significant role. For future research, we would like to extend our method to include occlusion, and use different BRDFs beyond microfacet models. Finally, we would like to continue refining the design of our prototype devices by replacing the external camera by an integrated sensor, paving the way for a true consumer acquisition device.

## Acknowledgements

We wish to thank the reviewers for their constructive feedback. Pieter Peers was partially funded by NSF grants: IIS-1217765, IIS-1350323, and a gift from Google.

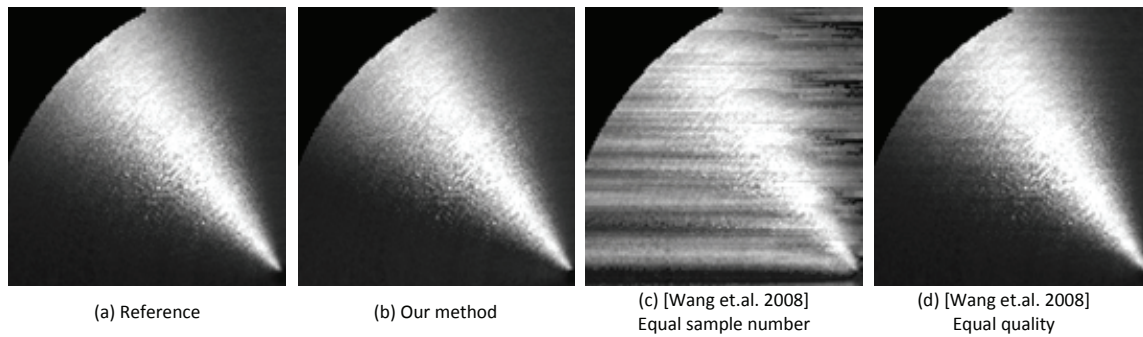


**Figure 13: Comparisons to Wang et al. [2008]** (a) Ground truth material under directional light source. (b) Re-rendering of reconstructions from 240 images captured with the desktop scanner (80 linear light source positions) (c) Re-rendering of reconstructions with an equal number of images (240) using the method of Wang et al. [2008] ( $15 \times 16$  LED light positions). (d) Re-rendering of equal quality reconstructions using the method of Wang et al. ( $80 \times 80$  images).

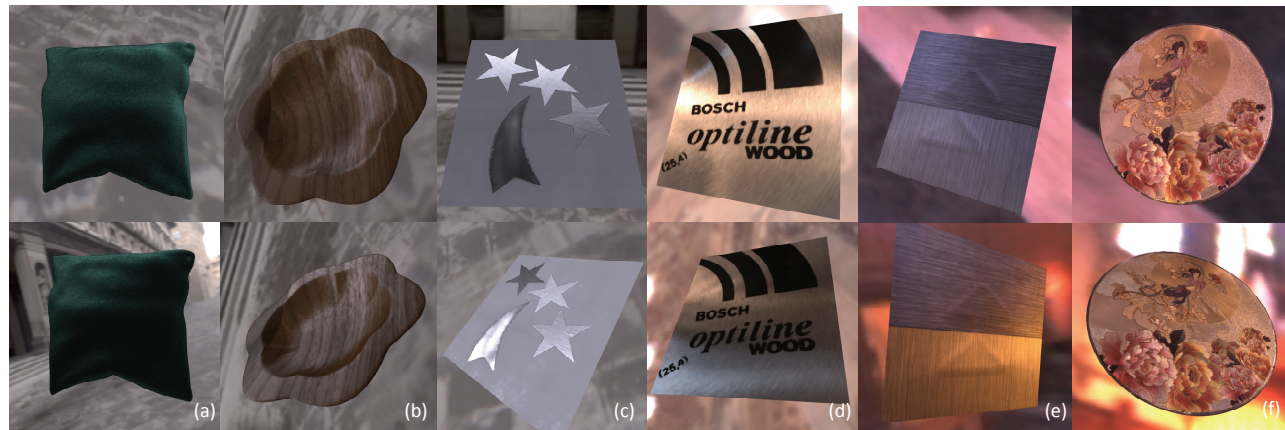


**Figure 14: Additional Results.** (a) Velvet. (b) Wood. (c) Paper and paint. (d) Brushed metal. (e) Bumpy anisotropic paper. (f) Circle card.

## References

- AITALA, M., WEYRICH, T., AND LEHTINEN, J. 2013. Practical SVBRDF capture in the frequency domain. *ACM Trans. Graph.* 32, 4.
- ALLDRIN, N., ZICKLER, T. E., AND KRIEGMAN, D. 2008. Photometric stereo with non-parametric and spatially-varying reflectance. In *CVPR*, 1–8.
- BEN-EZRA, M., WANG, J., WILBURN, B., LI, X., AND MA, L. 2008. An LED-only BRDF measurement device. In *CVPR*, 1–8.
- CAI, J.-F., CANDÈS, E. J., AND SHEN, Z. 2010. A Singular Value Thresholding Algorithm for Matrix Completion. *SIAM J. on Optimization* 20, 4, 1956–1982.
- COOK, R. L., AND TORRANCE, K. E. 1982. A reflectance model for computer graphics. *ACM Trans. Graph.* 1, 1, 7–24.
- DANA, K. J., NAYAR, S. K., VAN GINNEKEN, B., AND KOENDERINK, J. J. 1999. Reflectance and texture of real-world surfaces. *ACM Trans. Graph.* 18, 1, 1–34.
- DONG, Y., WANG, J., TONG, X., SNYDER, J., LAN, Y., BEN-EZRA, M., AND GUO, B. 2010. Manifold bootstrapping for svbrdf capture. *ACM Trans. Graph.* 29, 4, 98:1–98:10.
- GARDNER, A., TCHOU, C., HAWKINS, T., AND DEBEVEC, P. 2003. Linear light source reflectometry. *ACM Trans. Graph.* 22, 3, 749–758.
- GHOSH, A., CHEN, T., PEERS, P., WILSON, C. A., AND DEBEVEC, P. E. 2009. Estimating specular roughness and anisotropy from second order spherical gradient illumination. *Computer Graphics Forum* 28, 4, 1161–1170.
- GOLDMAN, D. B., CURLLESS, B., HERTZMANN, A., AND SEITZ, S. M. 2005. Shape and spatially-varying BRDFs from photometric stereo. In *ICCV*, I: 341–348.
- HAN, J. Y., AND PERLIN, K. 2003. Measuring bidirectional texture reflectance with a kaleidoscope. *ACM Trans. Graph.* 22, 3, 741–748.
- HOLROYD, M., LAWRENCE, J., HUMPHREYS, G., AND ZICKLER, T. 2008. A photometric approach for estimating normals and tangents. *ACM Trans. Graph.* 27, 5, 133:1–133:9.
- LAFORTUNE, E. P. F., FOO, S.-C., TORRANCE, K. E., AND GREENBERG, D. P. 1997. Non-linear approximation of reflectance functions. In *Proceedings of ACM SIGGRAPH 1997, Annual Conference Series*, 117–126.
- LAWRENCE, J., BEN-ARTZI, A., DECORO, C., MATUSIK, W., PFISTER, H., RAMAMOORTHY, R., AND RUSINKIEWICZ, S. 2006. Inverse shade trees for non-parametric material representation and editing. *ACM Trans. Graph.* 25, 3.

- LENSCH, H. P. A., KAUTZ, J., GOESELE, M., HEIDRICH, W., AND SEIDEL, H.-P. 2003. Image-based reconstruction of spatial appearance and geometric detail. *ACM Trans. Graph.* 22, 2, 234–257.
- LIU, G., LIN, Z., YAN, S., SUN, J., YU, Y., AND MA, Y. 2013. Robust Recovery of Subspace Structures by Low-Rank Representation. *IEEE PAMI* 35, 171–184.
- LU, R., KOENDERINK, J. J., AND KAPPERS, A. M. L. 1998. Optical properties bidirectional reflectance distribution functions of velvet. *Applied Optics* 37, 25 (Sept.), 5974–5984.
- MA, W.-C., HAWKINS, T., PEERS, P., CHABERT, C.-F., WEISS, M., AND DEBEVEC, P. E. 2007. Rapid acquisition of specular and diffuse normal maps from polarized spherical gradient illumination. In *Rendering Techniques*, 183–194.
- MARSCHNER, S., WESTIN, S., LAFORTUNE, E., TORRANCE, K., AND GREENBERG, D. 1999. Image-based BRDF measurement including human skin. In *10th Eurographics Rendering Workshop*.
- MATUSIK, W., PFISTER, H., BRAND, M., AND McMILLAN, L. 2003. Efficient isotropic BRDF measurement. In *Rendering Techniques*, 241–247.
- MUKAIGAWA, Y., SUMINO, K., AND YAGI, Y. 2007. High-speed measurement of BRDF using an ellipsoidal mirror and a projector. In *ACCV*, 246–257.
- NGAN, A., DURAND, F., AND MATUSIK, W. 2005. Experimental analysis of BRDF models. *Eurographics Symposium on Rendering 2005*, 117–226.
- NICODEMUS, F. E., RICHMOND, J. C., HSIA, J. J., GINSBERG, I. W., AND LIMPERIS, T. 1977. Geometric considerations and nomenclature for reflectance. *Monograph 161, National Bureau of Standards (US)*.
- NOCEDAL, J., AND WRIGHT, S. J. 2006. *Numerical Optimization*. Springer Series in Operations Research and Financial Engineering. Springer Science+Business Media, LLC.
- REN, P., WANG, J., SNYDER, J., TONG, X., AND GUO, B. 2011. Pocket reflectometry. *ACM Trans. Graph.* 30, 4, 45:1–45:10.
- TUNWATTANAPONG, B., FYFFE, G., GRAHAM, P., BUSCH, J., YU, X., GHOSH, A., AND DEBEVEC, P. E. 2013. Acquiring reflectance and shape from continuous spherical harmonic illumination. *ACM Trans. Graph.* 32, 4, 109.
- WANG, J., ZHAO, S., TONG, X., SNYDER, J., AND GUO, B. 2008. Modeling anisotropic surface reflectance with example-based microfacet synthesis. *ACM Trans. Graph.* 27, 3, 41:1–41:9.
- WARD, G. J. 1992. Measuring and modeling anisotropic reflection. In *Computer Graphics*, vol. 26, 265–272.
- ZHANG, Z. 2000. A flexible new technique for camera calibration. In *IEEE PAMI*, vol. 22, 1330–1334.
- ZICKLER, T., ENRIQUE, S., RAMAMOORTHI, R., AND BELHUMEUR, P. 2005. Reflectance sharing: image-based rendering from a sparse set of images. In *Rendering Techniques*, 253–264.